This is a preprint, the final version is subject to change, of the American Mineralogist (MSA)
Cite as Authors (Year) Title. American Mineralogist, in press.
(DOI will not work until issue is live.) DOI: http://dx.doi.org/10.2138/am-2016-5781CCBYNCND

Nanoscale gold clusters in arsenopyrite controlled by growth-rate not concentration: evidence from atom probe microscopy

Denis Fougerouse[1,2]*, Steven M. Reddy[1,2], David W. Saxey[1,3], William D.A. Rickard[1,3], Arie van Riessen[1,3], Steven Micklethwaite[4]

[1] *Geoscience Atom Probe, Advanced Resource Characterisation Facility, John de Laeter Centre, Curtin University, Perth, Western Australia, Australia*

[2] *Department of Applied Geology, Curtin University, Perth, Western Australia, Australia*

[3] *Department of Physics and Astronomy, Curtin University, Perth, Western Australia, Australia*

[4] *School of Earth, Atmosphere & Environment, Monash University, Melbourne, Victoria, Australia*

Corresponding author: denis.fougerouse@curtin.edu.au

Abstract

Auriferous sulfides, most notably pyrite (FeS_2) and arsenopyrite (FeAsS), are amongst the most important economic minerals on Earth because they can host large quantities of gold in many of the world's major gold deposits. Here we present the first atom probe study of gold distribution in arsenopyrite to characterize the three-dimensional (3D) distribution of gold at the nanoscale and provide data to discriminate among competing models for gold incorporation in refractory ores. In contrast to models that link gold distribution to gold concentration, gold incorporation in arsenopyrite is shown to be controlled by the rate of crystal growth, with slow growth-rate promoting the formation of gold clusters and rapid growth-rate leading to homogeneous gold distribution. This study yields new information on the controls of gold distribution and incorporation in sulfides that has important implications for ore deposit formation. More broadly this study reveals new information about crystal-fluid interface dynamics that determine trace element incorporation into growing mineral phases.

Introduction

Gold nanoparticles in undeformed arsenian pyrite and arsenopyrite have been inferred to form through four different mechanisms. Phase immiscibility during sulfide precipitation has been inferred from the correlation of gold particles with highly enriched domains (Reich et al., 2005), whereas the association of gold with randomly orientated polycrystalline sulfide is inferred to reflect post-crystallization gold exsolution during metamorphism (Palenik et al., 2004). Both of these models are strongly tied to the maximum gold solubility in arsenic-bearing sulfides. Above the maximum solubility limit, excess gold will precipitate as gold nanoparticles, whilst below the limit, gold will form a solid solution within the crystal lattice. In arsenopyrite, the maximum solubility for gold in solid solution has been estimated at ~2 wt.% using $C_{Au} = 0.02C_{As} + (4 \times 10^{-5})$ where C_{Au} and C_{As} represent the concentration of gold and arsenic respectively (Reich et al., 2005). The maximum gold solubility will decrease as temperature decreases, so exsolution of gold may take place during cooling and exhumation of the host rock (Palenik et al., 2004; Velásquez et al., 2014).

Observations by TEM of triangular gold nanoplates in supergene gold deposit indicate that colloidal nanoparticle solution is an active mechanism for gold transportation (Hough et al., 2011).

Hence, the formation of gold nanoparticles at depth, subsequent transportation in a fluid phase, and precipitation on the surface of sulfide minerals has been invoked as a potential mechanism for gold incorporation in arsenopyrite (Saunders, 1990; Hough et al., 2011).

A fourth model relies on the electrochemical and semiconducting properties of the sulfide surface and the ability for gold to adsorb from solution (Widler and Seward, 2002; Mikhlin et al., 2006; Becker et al., 2010). Gold adsorbed on to the host mineral surface, which initially bonds with the sulfide matrix, may diffuse and create covalent bonds with other gold atoms from neighboring adsorption sites or dissolved in solution. This process may lead to the formation of nanoparticles (Becker et al., 2010).

Discriminating between these different models has been difficult because the spatial and textural relationships amongst gold and sulfide phases at the nanoscale remains cryptic. X-ray absorption near-edge structure (XANES) analysis has demonstrated that gold atoms either bond with the crystal lattice as Au^{+} or exist as clusters in metallic Au^{0} form (Genkin et al., 1998; Simon et al., 1999; Cabri et al., 2000). High-resolution transmission electron microscopy combined with energy dispersive X-ray analysis (TEM-EDX) studies have recorded the occurrence and two-dimensional shape and distribution of metallic gold nanoparticles (Reich et al., 2005; Ciobanu et al., 2011; Deditius et al., 2011). However, the inability of older TEM-EDX systems to detect trace elements at low concentrations compromises the measurement of lattice-bound gold.

To address this issue and discriminate between the four competing models we have undertaken a combined synchrotron X-ray fluorescence microscopy (XFM) and atom probe microscopy study of gold-bearing arsenopyrite from the giant Paleoproterozoic Obuasi gold deposit, Ghana (Fougerouse et al., in press). Our results constrain the 3D distribution of gold at the nanoscale and provide new insights into the mechanisms of gold nanoparticle formation, which have implications for understanding gold mineralization processes.

Samples and methods

Sample Description

Approximately half of the mineralization (~30 MOz) in the Obuasi gold deposit is associated with arsenopyrite and occurred during peak upper greenschist metamorphism (T = 340-460°C, P = 2 kbars) of the ~ 2000 Ma Eburnean orogeny (Schwartz et al., 1992). The microchemistry and microstructure of these arsenopyrite ores has been studied in detail (Fougerouse et al., 2016a; Fougerouse et al., 2016b) providing a robust context for the atom probe study. In the arsenopyrite, gold is distributed in cyclic, submicron-scale bands (up to 100 bands) with sharp boundaries. The bands are concentric and parallel with the crystal boundaries and represent oscillatory crystallographic incorporation of gold into the crystal during growth (Fougerouse et al., 2016b).

X-ray fluorescence microscopy (XFM) mapping using the Maia detector

X-ray fluorescence mapping provides quantitative multi-element images with their full petrographic context (Dyl et al., 2014; Fisher et al., 2014). The analyses were performed at the XFM beamline at the Australian Synchrotron using the Maia 384 large angle detector array (Fisher et al., 2014). The samples were mapped with a pixel size of 2 microns and dwell time of 7.8125 ms for energies in the range 4–20 keV. Samples were prepared as polished thin sections (30 microns thick) mounted on 1 mm-thick quartz glass slides to minimize arsenic background from the glass slide. Standard foils (Mn, Fe, Pt and YF_3) were analyzed daily to calculate the X-ray flux and monitor drift. The Maia XFM full spectral data were analyzed using the GeoPIXE software suite. The Maia detector has a resolution of 400 eV which allows gold L-peaks to be distinguished in the spectra despite the peak overlap with arsenic K-peaks.

Atom probe sample preparation and analysis

Atom probe microscopy is a characterization technique with the unique ability to visualize the distribution of individual atoms in 3D (Kelly and Larson, 2012). The technique involves the application of a high voltage to a needle-shaped specimen, such that a very high electric field is generated at the specimen tip. In ‘laser assisted mode’, a laser pulse is focused on this high-field region, and provides sufficient thermal energy for atoms to be field-evaporated from the specimen and

undergo instantaneous ionization. The ionized atom or molecule is then accelerated through a local electrode aperture, and impacts on a position-sensitive detector. The ion trajectories are such that the quasi-hemispherical surface of the specimen is mapped onto the circular detector surface, with a magnification of approximately 10^6. In this way the original lateral (X,Y) location of the atom within the specimen needle can be determined from the detector impact location. Likewise, the depth (Z location) of the atom within the sample is determined from the order in which the atoms field-evaporate. Following the acquisition, the detection information is used to reconstruct the original 3D locations of each detected atom. Using time-of-flight mass spectrometry, the identity of the ion is determined from the time between the laser pulse and the detection event. Approximately 37% of the ions leaving the specimen are detected, with equal sensitivity across all elemental species. No pre-selection of elements is required prior to the analysis, and no standards are used to correct the data. Data quality, in terms of background noise, mass peak overlaps and detector saturation, is assessed from the data sets themselves, with uncertainties typically comparable to those arising from the counting statistics for each atomic species.

A region of interest (ROI) for atom probe specimens were selected from an inclusion free arsenopyrite crystal with variable, but high, gold contents (Fig. 1B). Two atom probe needle-shaped specimens were prepared and analyzed at the Advanced Resource Characterisation Facility at Curtin University. The ROI was extracted from the sample surface and prepared using a Tescan LYRA Focused Ion Beam Scanning Electron Microscope (FIB-SEM) with a Ga^+ ion source, employing standard lift-out techniques (Thompson et al., 2007).

A Cameca LEAP 4000X HR in laser assisted mode was used for the analyses. During the ~5 hour acquisitions, 15 million ions were collected from each of two specimens (specimen 1 and 2) at an evaporation rate of 0.01 ions/pulse, a UV laser (λ=355nm) energy of 45-50 pJ per pulse, and a pulse rate of 125 kHz. Specimens were maintained at a temperature of 55 K during data acquisition. The initial stages of data collection, involving optimization of the running parameters and specimen tip shaping, were removed from the final analysis. On the mass/charge spectra (supplementary materials Fig. SP1), peaks twice those of the background level were identified and ranged using the Cameca IVAS 3.6.10 processing software. The initial radius (R_i) of the specimen used for the 3D data

reconstruction was calculated from the radius after the experiment (R_f) using the equation: $R_i = (R_f \times V_i) / V_{f,}$,where V_i and V_f represent the voltage at the beginning and end of the analysis, respectively. Within the 3D reconstructed data, compositions of specific domains were isolated by volumes defined by concentration isosurfaces for clusters, and by cropping volumes for larger regions at constant voltage. In this study concentrations are reported in weight percent (wt.%) for major elements and weight part per million (ppm) for trace elements.

Results

The arsenopyrite crystals are hosted in sheared metasedimentary rocks composed of muscovite, quartz, chlorite and ankerite (Fig. 1). Synchrotron XFM shows that gold is distributed in cyclic and concentric bands that mimic the boundaries of the arsenopyrite crystals. Secondary nickel-enriched replacement domains (up to 2880 ppm nickel) cutting across the gold concentric zoning are developed around healed microfractures and grain boundaries and are the result of post-crystallization fluid-rock interactions. The depth penetration of the synchrotron XFM analysis reveals large metallic gold inclusions (~1 micron diameter) in the sub-surface of the sample often associated with micro-fractures. In an undeformed grain, both nickel-rich domains and large gold metallic inclusions were avoided during the atom probe sample preparation to specifically target the primary gold distribution.

The atom probe results indicate that the arsenopyrite composition is non-stoichiometric, being depleted in As and enriched in Fe and S (table 1). The major element composition of specimen 1 is relatively homogeneous across the length of the dataset. Specimen 1 has an average gold concentration of 724 ppm with the gold being segregated in isolated clusters up to 7 nm in diameter (Fig. 2). The clusters are oblate and spheroidal and follow the curvature of the evolving sample surface. The distribution of the clusters is heterogeneous across the specimen, with about 70 individual clusters imaged in the dataset. Clusters are spaced approximately 10 to 15 nm from each other. They are composed of several hundred atoms for the bigger clusters and only of 10 atoms for the smaller ones. The centermost of the largest cluster is composed of 46.7 wt.% gold. No other trace elements were found to be present in the clusters.

Specimen 2 comprises distinct compositional variations between two sub-domains separated by a continuous, sharp planar boundary (Fig. 2). A gold-rich (2,169 ppm) domain has a similar sulfur composition than sample 1, whereas an gold-poor domains (213 ppm) is arsenic-enriched and sulfur-depleted compared to the other domains analyzed (table 1; supplementary materials Fig. SP2). In each sub-domain of sample 2, the gold atoms are homogenously distributed and not clustered.

Discussion

The fine, epitaxial gold oscillatory zoning is interpreted to represent growth zones during a hydrothermal event rather than variation in the bulk fluid composition from separate hydrothermal events (Barker et al., 2009; Fougerouse et al., 2016b). The zones of higher gold concentration are associated with lower arsenic and higher sulfur contents, however the relationship between major element composition and gold incorporation remains unclear from our dataset. All analyzed arsenopyrite has gold concentrations less than the gold solubility limit in arsenopyrite of ~2 wt.%; (Reich et al., 2005).

Within domains defined by different gold concentrations, gold may be homogenously distributed or may form localized, flattened clusters. In specimen 1, the cluster distribution of gold is manifest as oblate and spheroidal clusters. Similar patterns have been reported for gold metal nanoparticles in magnesium oxide (Devaraj et al., 2014) and the unusual pattern of gold distribution is interpreted to be an atom probe reconstruction artifact associated with the contrast in evaporation field between the metallic gold nanoparticles and the arsenopyrite matrix. Such a contrast can lead to the development of topography at the specimen surface and this introduces trajectory aberrations manifest as dilution and magnification of the nanoparticles in the 3D reconstruction (Vurpillot et al., 2000) (Fig. 2C). The shape and composition of the gold clusters observed in the arsenopyrite specimen reported here are consistent with gold occurring as spherical metallic nanoparticles (Au^0). Therefore, domains containing gold nanoparticles (Au^0) and others where gold is homogeneously distributed in the sulfide lattice, most likely as Au^+ species (Cabri et al., 2000), are reported in a single arsenopyrite crystal only a few microns apart. The absence of clusters in specimen 2 is inconsistent with gold being

transported in hydrothermal fluids as colloidal gold nanoparticles (Saunders, 1990; Hough et al., 2011).

Gold clusters in specimen 1 are only associated with intermediate concentrations (724 ppm) an order of magnitude below the gold solubility limit in arsenopyrite of ~20,000 ppm. Therefore, the phase immiscibility model (Reich et al., 2005), though potentially explaining the formation of gold nanoparticles above the gold solubility limit in solid-solution with arsenic-bearing sulfides, is not consistent with the formation of nanoparticles in specimen 1. In addition, both gold-enriched (2,169 ppm) and gold-poor (213 ppm) domains of specimen 2 are cluster free. These data show that there is no systematic relationship between the presence of gold clusters and gold concentration in arsenopyrite and there is no evidence for the formation of gold nanoparticles being controlled by the maximum gold solubility in arsenopyrite (Reich et al., 2005).

The atom probe specimens come from only a few microns apart and therefore are assumed to have experienced a common metamorphic history. Hence, the difference in gold distribution is unlikely to be a result of temperature-controlled post-crystallisation remobilization of gold due to changing gold solubility during exhumation (Palenik et al., 2004). The lack of a temperature control on the formation of gold nanoclusters highlights a need for caution when using nanoparticle occurrence and size as an indicator of formation temperature (Reich et al., 2006).

Experimental and thermodynamic studies of gold adsorption on sulfide surfaces indicate that the formation of metallic Au^0 and Au–Au bonds are more energetically favorable than bonds between Au^+ and the sulfide matrix (Mikhlin et al., 2006; Becker et al., 2010). As a result, Au^+ ions have the ability to diffuse at the crystal surface, or “hop”, from adsorption sites to form Au^0 dimers, initiating clusters that coarsen with time (Becker et al., 2010). In this case, the expectation is that most gold would be distributed in nanoparticulate form and that increasing gold concentrations would be associated with increasing nanoparticle size. This is not consistent with the absence of gold nanoparticles in the high concentration area of specimen 2 and another control on the ability of gold to diffuse on the crystal surface must be significant. One possible control is growth rate since slow crystal growth rate increases the residence time of the Au^+ ions at the sulfide surface, and thus increases the ability of Au^+ ions to diffuse on the crystal surface from one adsorption site to another.

As a result, more energetically favorable Au-Au bonds can form, leading to the growth of *in situ* Au^0 nanoparticles (Becker et al., 2010). Conversely, a fast growth-rate and short residence time for the Au^+ ions at the sulfide surface limits the diffusion of Au^+ ions on the sulfide surface and promotes the gold trapping and encapsulation within the growing arsenopyrite (Fig. 3). The presented data are consistent with a model in which formation of gold nanoparticles in controlled by crystal growth rate. Analogous mechanisms for variation of trace element concentration with crystal growth rate have been reported for experimental data in calcite (Watson, 2004; Barker and Cox, 2011).

In this study, synchrotron XFM multi-element mapping has provided the textural framework for detailed analysis of gold distribution at the nanoscale. The innovative use of atom probe microscopy has captured variations in the distribution of gold that is far more complex than previously reported and allows testing of competing models for nanoscale gold cluster formation in arsenopyrite. The atom probe data are only consistent with a growth-rate control on gold cluster formation in arsenopyrite such that faster growth rates promoting homogenous gold incorporation whilst slower rates induce the formation of nanoparticles by surface diffusion. Our results illustrate that a systematic atom probe investigation of the crystal chemistry of arsenopyrite has the potential to reveal the nanoscale distribution of gold and resolve the mechanisms responsible for these distributions. Such information has the potential to enhance gold recovery and improve the optimization of the mineral processing workflow from refractory ores. The results may also have importance for understanding the mechanisms of trace element incorporation in other crystallizing minerals. More generally, our results illustrate that the further development and application of atom probe microscopy has the potential to provide the constraints needed to discriminate among contentious geochemical processes in a range of geological materials..

Acknowledgments

The Australian Resource Characterisation Facility (ARCF), under the auspices of the National Resource Sciences Precinct (NRSP) – a collaboration between CSIRO, Curtin University and The University of Western Australia – is supported by the Science and Industry Endowment Fund. This is contribution XXX from The Institute for Geoscience Research (TIGeR). Components of this research

were undertaken on the X-ray fluorescence microscopy beamline at the Australian Synchrotron, Victoria, Australia. The data presented in this paper were collected as part of run 6666. This manuscript benefitted from careful reviews by Shaun Barker, Nigel Cook and Alberto Perez-Huerta.

References

Barker, S.L., and Cox, S.F. (2011) Oscillatory zoning and trace element incorporation in hydrothermal minerals: insights from calcite growth experiments. Geofluids, 11(1), 48-56.

Barker, S.L., Hickey, K.A., Cline, J.S., Dipple, G.M., Kilburn, M.R., Vaughan, J.R., and Longo, A.A. (2009) Uncloaking invisible gold: use of nanoSIMS to evaluate gold, trace elements, and sulfur isotopes in pyrite from Carlin-type gold deposits. Economic Geology, 104(7), 897-904.

Becker, U., Reich, M., and Biswas, S. (2010) Nanoparticle–host interactions in natural systems. In F. Brenker, and G. Jordan, Eds. Nanoscopic Approaches in Earth and Planetary Sciences: EMU Notes in Mineralogy, 8, p. 1-52.

Cabri, L.J., Newville, M., Gordon, R.A., Crozier, E.D., Sutton, S.R., McMahon, G., and Jiang, D.-T. (2000) Chemical speciation of gold in arsenopyrite. The Canadian Mineralogist, 38(5), 1265-1281.

Ciobanu, C., Cook, N., Utsunomiya, S., Pring, A., and Green, L. (2011) Focussed ion beam–transmission electron microscopy applications in ore mineralogy: Bridging micro-and nanoscale observations. Ore Geology Reviews, 42(1), 6-31.

Deditius, A.P., Utsunomiya, S., Reich, M., Kesler, S.E., Ewing, R.C., Hough, R., and Walshe, J. (2011) Trace metal nanoparticles in pyrite. Ore Geology Reviews, 42(1), 32-46.

Devaraj, A., Colby, R., Vurpillot, F.o., and Thevuthasan, S. (2014) Understanding atom probe tomography of oxide-supported metal nanoparticles by correlation with atomic-resolution electron microscopy and field evaporation simulation. The Journal of Physical Chemistry Letters, 5(8), 1361-1367.

Dyl, K.A., Cleverley, J.S., Bland, P.A., Ryan, C.G., Fisher, L.A., and Hough, R.M. (2014) Quantified, whole section trace element mapping of carbonaceous chondrites by Synchrotron X-ray

Fluorescence Microscopy: 1. CV meteorites. Geochimica et Cosmochimica Acta, 134(0), 100-119.

Fisher, L.A., Fougerouse, D., Cleverley, J.S., Ryan, C.G., Micklethwaite, S., Halfpenny, A., Hough, R.M., Gee, M., Paterson, D., and Howard, D.L. (2014) Quantified, multi-scale X-ray fluorescence element mapping using the Maia detector array: application to mineral deposit studies. Mineralium Deposita, 1-10.

Fougerouse, D., Micklethwaite, S., Halfpenny, A., Reddy, S.M., Cliff, J.B., Martin, L.A.J., Kilburn, M., Guagliardo, P., and Ulrich, S. (2016a) The golden ark: arsenopyrite crystal plasticity and the retention of gold through high strain and metamorphism. Terra Nova, n/a-n/a.

Fougerouse, D., Micklethwaite, S., Tomkins, A.G., Mei, Y., Kilburn, M., Guagliardo, P., Fisher, L.A., Halfpenny, A., Gee, M., Paterson, D., and Howard, D.L. (2016b) Gold remobilisation and formation of high grade ore shoots driven by dissolution-reprecipitation replacement and Ni substitution into auriferous arsenopyrite. Geochimica et Cosmochimica Acta, 178, 143-159.

Fougerouse, D., Micklethwaite, S., Ulrich, S., Miller, J., McCuaig, T.C., Godel, B., and Adams, D. (in press) Evidence for Two Stages of Mineralization in West Africa's Largest Gold Deposit: Obuasi, Ghana. Economic Geology.

Genkin, A.D., Bortnikov, N.S., Cabri, L.J., Wagner, F., Stanley, C.J., Safonov, Y.G., McMahon, G., Friedl, J., Kerzin, A.L., and Gamyanin, G.N. (1998) A multidisciplinary study of invisible gold in arsenopyrite from four mesothermal gold deposits in Siberia, Russian Federation. Economic Geology, 93(4), 463-487.

Hough, R.M., Noble, R.R.P., and Reich, M. (2011) Natural gold nanoparticles. Ore Geology Reviews, 42(1), 55-61.

Kelly, T.F., and Larson, D.J. (2012) Atom probe tomography 2012. Annual Review of Materials Research, 42, 1-31.

Mikhlin, Y.L., Romanchenko, A.S., and Asanov, I.P. (2006) Oxidation of arsenopyrite and deposition of gold on the oxidized surfaces: A scanning probe microscopy, tunneling spectroscopy and XPS study. Geochimica et cosmochimica acta, 70(19), 4874-4888.

Palenik, C.S., Utsunomiya, S., Reich, M., Kesler, S.E., Wang, L., and Ewing, R.C. (2004) "Invisible „gold revealed: Direct imaging of gold nanoparticles in a Carlin-type deposit. American Mineralogist, 89(10), 1359-1366.

Reich, M., Kesler, S.E., Utsunomiya, S., Palenik, C.S., Chryssoulis, S.L., and Ewing, R.C. (2005) Solubility of gold in arsenian pyrite. Geochimica et Cosmochimica Acta, 69(11), 2781-2796.

Reich, M., Utsunomiya, S., Kesler, S.E., Wang, L., Ewing, R.C., and Becker, U. (2006) Thermal behavior of metal nanoparticles in geologic materials. Geology, 34(12), 1033-1036.

Saunders, J.A. (1990) Colloidal transport of gold and silica in epithermal precious-metal systems: Evidence from the Sleeper deposit, Nevada. Geology, 18(8), 757-760.

Schwartz, M.O., Oberthür, T., Amanor, J., and Gyapong, W.A. (1992) Fluid inclusion re-equilibration and P-T-X constraints on fluid evolution in the Ashanti gold deposit, Ghana. European Journal of Mineralogy, 4(5), 1017-1033.

Simon, G., Huang, H., Penner-Hahn, J.E., Kesler, S.E., and Kao, L.-S. (1999) Oxidation state of gold and arsenic in gold-bearing arsenian pyrite. American mineralogist, 84, 1071-1079.

Thompson, K., Lawrence, D., Larson, D., Olson, J., Kelly, T., and Gorman, B. (2007) In situ site-specific specimen preparation for atom probe tomography. Ultramicroscopy, 107(2), 131-139.

Velásquez, G., Béziat, D., Salvi, S., Siebenaller, L., Borisova, A.Y., Pokrovski, G.S., and De Parseval, P. (2014) Formation and deformation of pyrite and implications for gold mineralization in the El Callao District, Venezuela. Economic Geology, 109(2), 457-486.

Vurpillot, F., Bostel, A., and Blavette, D. (2000) Trajectory overlaps and local magnification in three-dimensional atom probe. Applied Physics Letters, 76(21), 3127-3129.

Watson, E.B. (2004) A conceptual model for near-surface kinetic controls on the trace-element and stable isotope composition of abiogenic calcite crystals. Geochimica et Cosmochimica Acta, 68(7), 1473-1488.

Widler, A., and Seward, T. (2002) The adsorption of gold (I) hydrosulphide complexes by iron sulphide surfaces. Geochimica et Cosmochimica Acta, 66(3), 383-402.

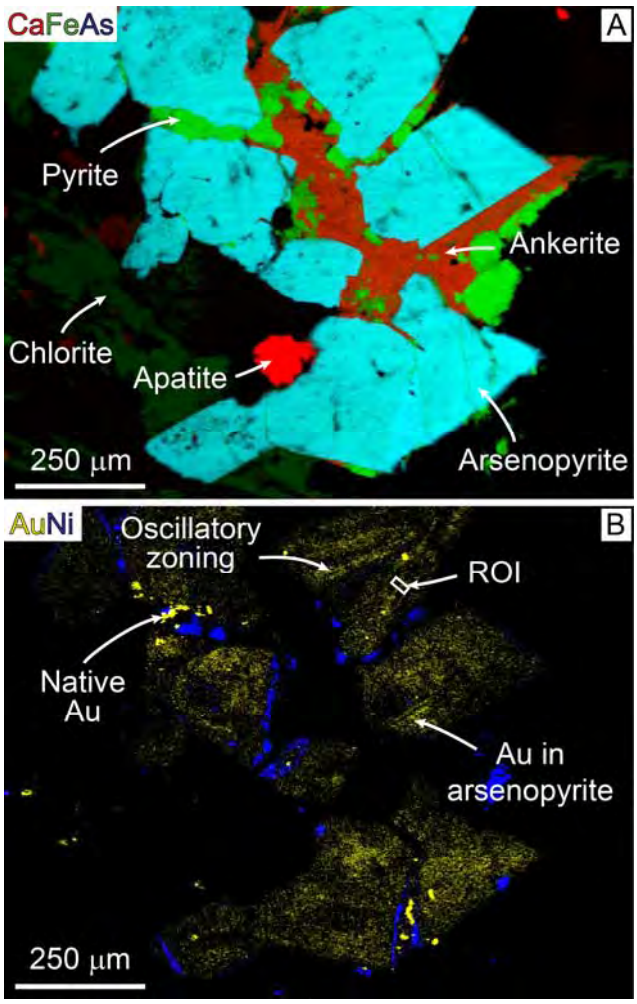

314

315 Figure 1: Synchrotron XFM RGB images of an arsenopyrite in sample 215-7b. (A) Major element
316 distribution (red = Ca; Green = Fe; Blue = As). (B) Trace element distribution (yellow = Au; blue =
317 Ni) showing epitaxial gold zonation surrounding gold-poor cores. The region of interest (ROI) for the
318 atom probe study is shown. Modified after Fisher et al (2015).

319

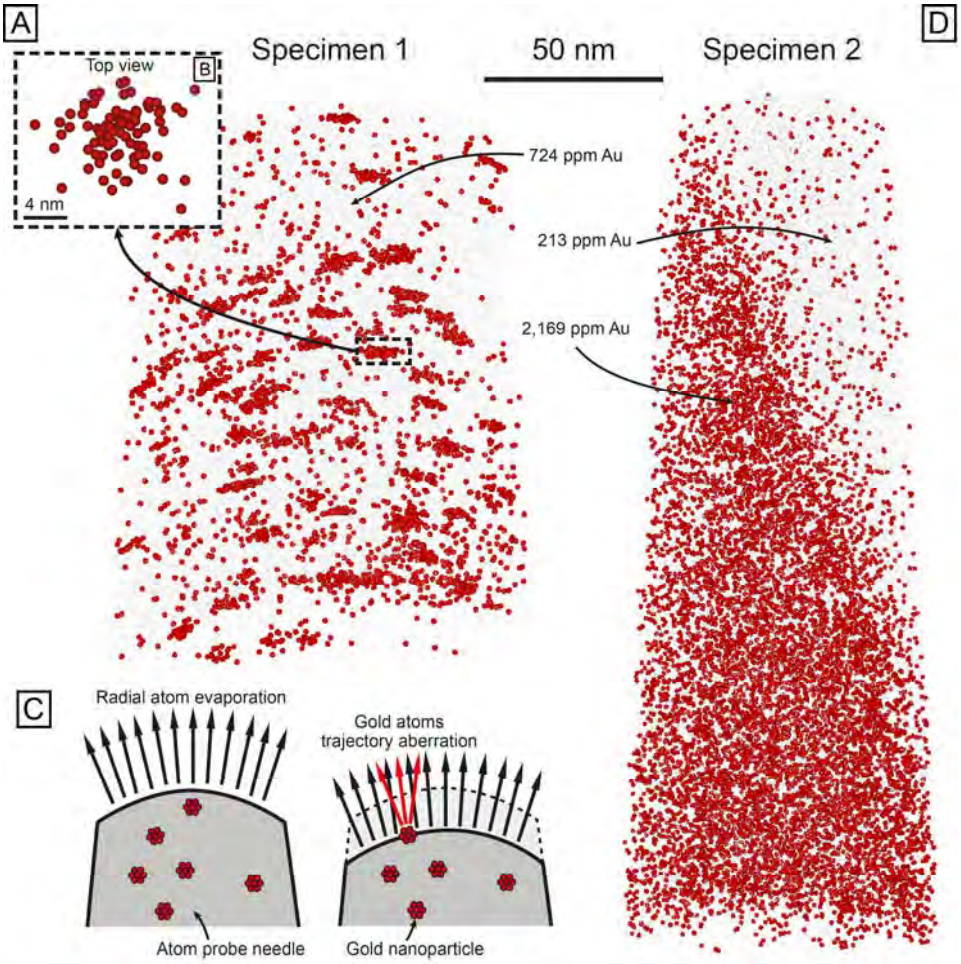

Figure 2: Atom probe results. Gold atoms are displayed as red spheres. (A) Specimen 1. Gold atoms are segregated in clusters; (B) 5 nm slice through the largest gold cluster; (C) Interpretative diagram showing the apparent local magnification of the data, arising from trajectory aberrations around high-evaporation field nanoparticles, which protrude from the surface of the sample; (D) Specimen 2. The distribution of gold atoms is divided in two domains. The gold within each domain is homogeneously distributed.

328 Table 1: Table of major and trace element compositions measured by atom probe microscopy from all

329 arsenopyrite domains.

	Fe (wt.%)	As (wt.%)	S (wt.%)	Au (ppm)
Specimen 1 bulk	36.3	42	21.5	724
Specimen 2 gold-rich domain	37.1	41.1	21.5	2169
Specimen 2 gold-poor domain	37	42.1	20.8	213

330

331

This is a preprint, the final version is subject to change, of the American Mineralogist (MSA)
Cite as Authors (Year) Title. American Mineralogist, in press.
(DOI will not work until issue is live.) DOI: http://dx.doi.org/10.2138/am-2016-5781CCBYNCND

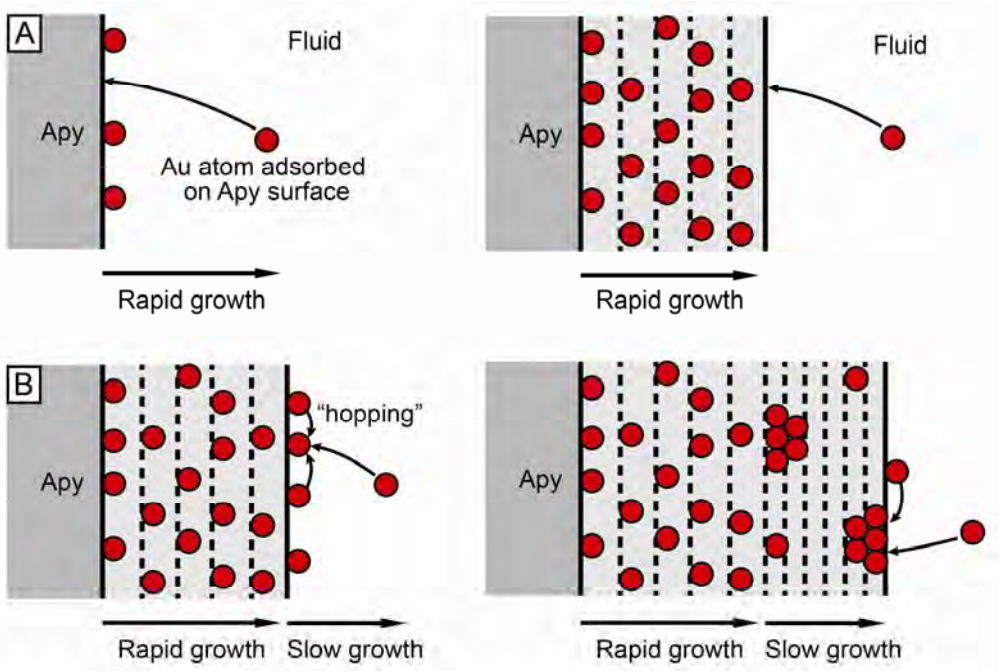

Figure 3: Interpretative diagram illustrating the effect of the crystal growth-rate on the gold distribution. Rapid growth results in high gold concentration homogeneously distributed whereas slow growth facilitates surface diffusion and formation of nanoparticles.